Deep–Sea Research II 169-170 (2019) 104680

Contents lists available at ScienceDirect

Deep-Sea Research Part II

journal homepage: http://www.elsevier.com/locate/dsr2

Spatio-temporal variability of surface water pCO_2 and nutrients in the tropical Pacific from 1981 to 2015

S. Yasunaka [a,*], S. Kouketsu [a], P.G. Strutton [b,c], A.J. Sutton [d], A. Murata [a], S. Nakaoka [e], Y. Nojiri [e]

[a] Research Institute for Global Change, Japan Agency for Marine-Earth Science and Technology, Yokosuka, Japan
[b] Institute for Marine and Antarctic Studies, University of Tasmania, Hobart, Tasmania, Australia
[c] Australian Research Council Centre of Excellence for Climate Extremes, University of Tasmania, Hobart, Tasmania, Australia
[d] Pacific Marine Environmental Laboratory, National Oceanic and Atmospheric Administration, Seattle, WA, USA
[e] Center for Global Environmental Research, National Institute for Environmental Studies, Tsukuba, Japan

A B S T R A C T

This study presents a synthesis of surface water partial pressure of CO_2 (pCO_2) and nutrient observations in the tropical Pacific (20°S–20°N) from 1981 to 2015 and characterizes the spatio-temporal variability. We used data from the Surface Ocean CO_2 Atlas version 5, which include about 2 million pCO_2 measurements in the tropical Pacific. Unlike many previous studies that estimated pCO_2 fields from relationships with other variables like sea surface temperature, we developed gridded products of monthly means using a technique to interpolate measured pCO_2 values. Large seasonal variation of pCO_2 appears in the cold tongue region (EQ–20°S, east of 120°W) corresponding to the seasonal variation of coastal upwelling, and in the off-equatorial region where the thermodynamic effect on pCO_2 dominates. Consistent with previous findings, pCO_2 along the equator declines during El Niño due to weakening of the easterly winds and therefore reduced upwelling of CO_2 rich subsurface water. We also quantified the spatial distribution of the long-term pCO_2 trend beyond the area-averaged trend presented previously. The long-term trend of pCO_2 is positive in all regions with an area average of 1.8 ± 0.1 µatm yr^{-1}. However, along the equator the trend is > 2 µatm yr^{-1} linked to the Pacific Decadal Oscillation forcing. Using the same methodology, we also analyzed about 20,000 surface nutrient measurements from the Global Ocean Data Analysis Project version 2, World Ocean Database 2013, and ship-of-opportunity sampling by the National Institute for Environmental Studies, Japan. We present the spatial patterns of reduced surface nutrient concentration in the central to eastern tropics along the equator during El Niño, but there are not enough data to characterize the trends of nutrients in the tropical Pacific.

Decorrelation analyses are also applied using covariance between pCO_2 anomalies separated by a lag increment for zonal, meridional, and temporal directions. The e-folding scale of pCO_2 is estimated to be 6° in latitude, 13° in longitude, and 2 months with a signal-to-noise ratio of 4, which are used as input for the interpolation as well as an assessment of ideal observation density and frequency. Decorrelation analyses such as this are critical for evaluating existing observing system design and informing future sampling strategies.

1. Introduction

The tropical Pacific is characterized by the warm pool in the west and the cold tongue in the east. In the cold tongue region, the upwelled water is cool and rich in dissolved inorganic carbon (DIC) and nutrients, but iron-limited, which causes moderate productivity and strong CO_2 release to the atmosphere (Chavez and Barber, 1987; Feely et al., 1987). The position of the warm pool and the cold tongue fluctuates seasonally and interannually (Horel, 1982; Rasmusson and Carpenter, 1982; McPhaden and Picaut, 1990; Yan et al., 1992). Interannual fluctuation is associated with El Niño-Southern Oscillation (ENSO). During El Niño, upwelling weakens and the cold tongue retreats to the east. As a result, nutrient concentrations along the equator tend to be lower (Strutton et al., 2008), and the equatorial CO_2 outgassing in the tropics weakens and sometimes ceases completely (Feely et al., 1997; Ishii et al., 2014).

The temporal variation of surface ocean partial pressure of CO_2 (pCO_2) and air-sea CO_2 flux along the equator, and their spatial distribution for specific years have been presented by many studies (Feely et al., 1995, 1997, 1999, 2002, 2006; Takahashi et al., 2003; Ishii et al., 2009; Sutton et al., 2014). Previous studies have also shown contrasting ENSO signals between eastern and western tropics (Patra et al., 2005; Ishii et al., 2014; Rödenbeck et al., 2015) and changes in decadal trends (Takahashi et al., 2003; Feely et al., 2006; Ishii et al., 2009, 2014). Most of the observation-based estimates employed statistical relationship between pCO_2 and other variables, such as sea surface temperature (SST). However, these relationships are not uniform in time or space. Assuming consistent relationships across time and space scales, or classifying wide areas including coastal zones into the same biome, may

* Corresponding author.
E-mail address: yasunaka@jamstec.go.jp (S. Yasunaka).

https://doi.org/10.1016/j.dsr2.2019.104680
Received 15 October 2018; Received in revised form 6 October 2019; Accepted 21 October 2019
Available online 31 October 2019

cause uncertainties (Wanninkhof et al. 2013; Wang et al., 2015). Although various statistical estimates and biogeochemical model simulations of CO_2 are qualitatively consistent when they are averaged over the tropical Pacific and for the several decades (Ishii et al., 2014; Rödenbeck et al., 2015), temporal variation shows substantial differences (Rödenbeck et al., 2015) and difference in spatial variation has not been presented yet. Furthermore, spatio-temporal variations of CO_2 in models are still biased (Wang et al., 2006; Valsala et al., 2014) and underlying mechanisms controlling the variations are different (Jiang and Chai, 2006). In terms of nutrients, spatio-temporal variability has not been characterized yet even at the surface.

This study synthesizes sea surface pCO_2 and nutrient observations in the tropical Pacific (20°S–20°N) from 1981 to 2015, and grids them using interpolation. For the interpolation, we estimate e-folding scales and signal-to-noise ratios by measured values themselves, instead of any pre-assumed relationships with other explaining parameters. Using the gridded products, we characterize pCO_2 and nutrient basin-scale spatio-temporal variabilities.

To enhance and redesign internationally-coordinated observations of the tropical Pacific, the Tropical Pacific Observing System 2020 project (TPOS2020; tpos2020.org) was initiated in 2014. Gasparin et al. (2015) showed that existing oceanographic observations by moored buoys, satellite altimeters and Argo floats can represent the intra-seasonal to interannual variability in temperature, salinity and sea surface height. Focusing on biogeochemical variables, we present the current and historical state of the observing system for sea surface pCO_2 and macro-nutrient observations and characterize the spatio-temporal variabilities captured by those observations.

2. Data

We used surface water pCO_2 mearsurements (converted from the fugacity of CO_2 values; a correction of <1%) from the Surface Ocean CO_2 Atlas version 5 (SOCATv5; Bakker et al., 2016; http://www.socat.info/). The total number of measurements in the tropical Pacific (20°S–20°N) from 1981 to 2015, is about 2 million (Fig. 1). Almost all 1° grid cells are populated with measurements, especially along Tropical Atmosphere Ocean (TAO) array mooring longitudes serviced by the National Oceanic and Atmospheric Administration (NOAA), US (Feely et al., 2006), along the ship of opportunity (SOO) line between Japan and New Zealand occupied by National Institute for Environmental Studies, Japan (NIES; Nakaoka et al., 2013), and along SOO line between Long Beach and New Zealand by NOAA (Quay et al., 2009) (Fig. 1a). The number of the mearsurements increased in the early-1990s when routine NOAA observations along TAO arrays were started, and then in the mid-2000s when SOO observations by NIES and NOAA were started (Fig. 1b).

Surface nutrient (phosphate, nitrate, and silicate) measurements obtained from water depths shallower than 10 m were extracted from the Global Ocean Data Analysis Project version 2 (GLODAPv2; Olsen et al., 2016) and the World Ocean Database 2013 (Boyer et al., 2013). Duplicates with data archived in GLODAPv2 were excluded from WOD13. We also used surface samples of nutrients collected by the NIES (Yasunaka et al., 2014). The total number of measurements is about 20,000 of each variable. Repeated observations are limited mainly to the 137°E and 165°E lines occupied by Japan Meteorological Agency (Oka et al., 2017), along the SOO ship route between Japan and New Zealand by NIES (Yasunaka et al., 2014), and in the coastal region of South America by Instituto del Mar del Peru (Echevin et al., 2008, Fig. 2a). The density of the data is around the same level from the 1980s to recent years (Fig. 2b). The numbers of phosphate and silicate samples are similar to that of nitrate throughout the analysis period.

SST data were obtained from Hadley Centre Sea Ice and Sea Surface Temperature data set (HadISST) with a $1° \times 1°$ monthly resolution (Rayner et al., 2003; https://www.metoffice.gov.uk/hadobs/hadisst/). Sea surface salinity (SSS) data were obtained from quality controlled ocean temperature and salinity monthly objective analyses version 4 by the Met Office Hadley Centre (EN4; https://www.metoffice.gov.uk/hadobs/en4/; Good et al., 2013). Zonal mean data for the atmospheric CO_2 mixing ratio (xCO_2) were retrieved from the NOAA Greenhouse Gas Marine Boundary Layer Reference data product (Conway et al., 1994; http://www.esrl.noaa.gov/gmd/ccgg/mbl/index.html) and were interpolated into $1° \times 1° \times 1$ month grid-cells. Sea level pressure, 6-hourly 10-m wind speed data, and zonal wind data were obtained from the U.S. National Centers for Environmental Prediction–Department of Energy Reanalysis 2 (NCEP2) (Kanamitsu et al., 2002; http://www.esrl.noaa.gov/psd/data/gridded/data.ncep.reanalysis2.html).

As a comparison with our gridded products, we used the seawater pCO_2 gridded products by Landschützer et al. (2016; https://www.nodc.noaa.gov/ocads/oceans/SPCO2_1982_present_ETH_SOM_FFN.html; ETH_SOM-FFN) and Iida et al. (2015; http://www.data.jma.go.jp/gmd/kaiyou/english/co2_flux/co2_flux_data_en.html; JMA_MLR). ETH_SOM-FFN was estimated by a combined two-step neural network (a self-organizing map and a feed-forward network) approach with SST, SSS, mixed layer depth, and chlorophyll-a. JMA_MLR was estimated using multiple linear regression of SST, SSS, and chlorophyll-a. We also used nutrient climatologies from World Ocean Atlas 2013 (WOA13) (Garcia et al., 2014; https://www.nodc.noaa.gov/OC5/woa13/), which

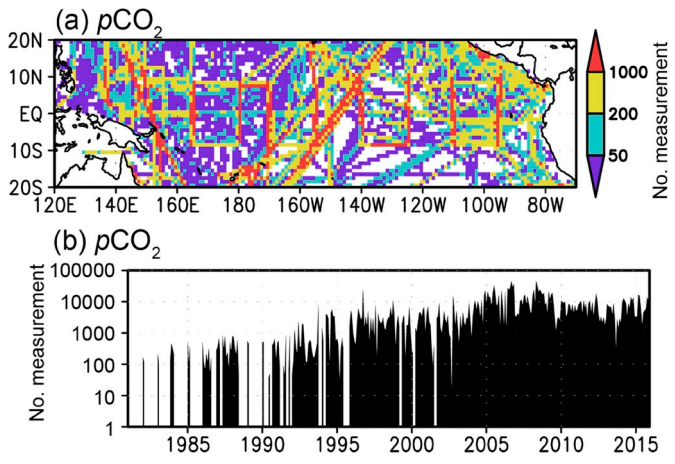

Fig. 1. (a) Spatial and (b) temporal distribution of number of surface seawater pCO_2 measurements in SOCATv5. (a) The total number of measurements in each 1° grid cell between 1981 and 2015. (b) The total number of measurements each month in the tropical Pacific (20°S–20°N, 120°E–70°W).

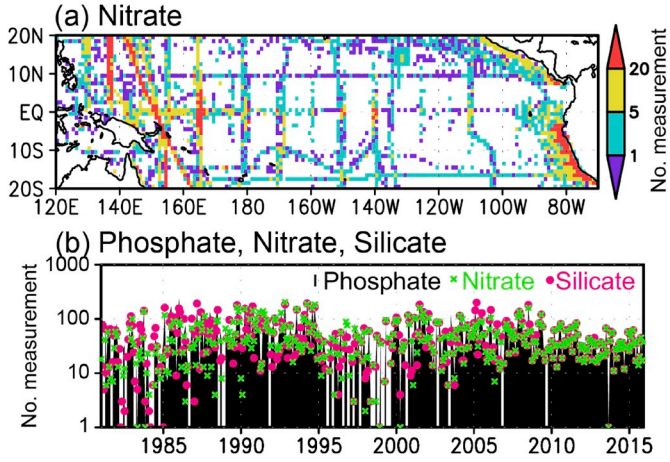

Fig. 2. (a) Spatial distribution of the number of surface nitrate measurements and (b) temporal distribution of nutrient measurements in GLODAPv2, WOD2013, and NIES VOS program. (a) The total number of measurements in each 1° grid cell between 1981 and 2015. (b) The total number of measurements each month in the tropical Pacific (20°S–20°N, 120°E–70°W).

were made by an interpolation of observations.

3. Methods

3.1. Gridding of pCO_2 and nutrient measurements

We averaged the surface water pCO_2 measurements onto $1^\circ \times 1^\circ$ monthly grid boxes for each year from 1981 to 2015 with statistical quality control to assure the gridded data were not affected by erroneous measurements or short-term and small-scale extreme conditions. We did this after normalizing pCO_2 to the reference year 2005 based on changes in the atmospheric CO_2, as done by Takahashi et al. (2002) to avoid bias in the long-term mean field. Separate treatment of the long-term trend also avoids reduction of the long-term trend in the resultant data from optimal interpolation (Reynolds and Smith, 1994). As reference values for quality control, we calculated the long-term monthly mean and its standard deviation for each $1^\circ \times 1^\circ$ grid-cell. Window size for the mean was set to $\pm 2^\circ$ of latitude, $\pm 5^\circ$ of longitude, and ± 1 month (regardless of the year) for pCO_2, and $\pm 5^\circ$ of latitude, $\pm 15^\circ$ of longitude, and ± 2 months for nutrients. The size of the window was set so that the number of measurements in the window was at least 100. We then eliminated measurements in each grid-cell that differed by more than three standard deviations from the long-term mean. We again calculated the long-term mean and its standard deviation, and eliminated measurements that differed from the long-term mean by more than three standard deviations. This procedure identified in total about 0.5% of the measurements as extreme values. These excluded measurements were randomly distributed in time and space, except for some in the coastal region because of the locally high values. Finally, the remaining measurements were binned into $1^\circ \times 1^\circ \times 1$ month grid-cells from 1981 to 2015.

3.2. Calculation of monthly climatology

We calculated long-term monthly means of the quality-controlled gridded data obtained in section 3.1, and smoothed them by the exponentially weighted average with the same space and time constants as the window size used in section 3.1. We use the monthly climatologies for detecting the seasonal variation, and also as reference values to calculate anomalies for detecting the interannual variability.

For SST, we calculated long-term monthly means by averaging monthly SSTs from 1981 to 2015.

3.3. Decorrelation analysis

By using pCO_2 anomalies of the quality-controlled gridded data obtained in section 3.1 from the monthly climatology in section 3.2, we calculated the data covariance at each $1^\circ \times 1^\circ$ grid cell separated by a lag increment in the zonal, meridional, and temporal directions. Covariance at a latitude of la and a longitude of lo (Cov(la, lo)) in meridional direction are calculated by

$$\mathrm{Cov(la, lo)} = < \mathrm{X(la, lo, im)\ X(la + \Delta la, lo, im)} >$$

where X(la, lo, im) is pCO_2 anomaly at a latitude of la, a longitude of lo, and a month of im, Δla is a lag increment in the meridional direction, and $< >$ is an average from January 1981 to December 2015. Cov(la, lo) in the zonal direction was calculated using X(la, lo, im) and X(la, lo + Δlo, im), and in time using X(la, lo, im) and X(la, lo, im + Δim). In the figures, we show normalized covariance, which is normalized to variance of monthly anomalies (i.e. the correlation coefficient).

Decorrelation radius and signal-to-noise ratio can be obtained from the lag covariance. The covariance decays with increasing lag. We defined decorrelation radius as the constant value of the best fitted exponential decay line on the lag covariance. The covariance at lag 0 is the sum of the signal and noise variance, and the covariance at other lags is just the signal variance (Alaka and Elvander, 1972). Therefore, the difference in covariance between lag 0 and a very short lag approximately represents the noise variance. In our case, we used the difference between lag 0 and the minimum lags (i.e. 1° in zonal and meridional directions and 1 month in temporal direction).

3.4. Optimal interpolation

We applied optimal interpolation to the quality-controlled monthly data obtained in Section 3.1. Hosoda et al. (2008) presented detailed equations for the optimal interpolation used here. We used the monthly climatology obtained in Section 3.2 as the first guess. We also used the decorrelation radius and signal-to-noise ratio obtained from the covariance analysis in Section 3.3. For nutrients, the decorrelation radius and signal-to-noise ratio of pCO_2 were used since the decorrelation radius and signal-to-noise ratio of nutrients could not be retained due to lack of data (see Section 4.2.1). Window sizes for calculation of covariance matrices were set to be twice the size of the decorrelation radius. Finally, for pCO_2, we added the atmospheric CO_2 change initially subtracted (see Section 3.1). As a result, pCO_2 and nutrient monthly values and the interpolation errors are obtained. We used these products to characterize the pCO_2 and nutrient interannual variabilities. For an easy comparison of the interpolation errors in time and space, the interpolation errors are normalized to the monthly anomalies at each grid point.

3.5. Regression analysis

To examine seawater pCO_2 and nutrient variabilities associated with ENSO, we show their regression patterns with the Niño 3.4 index, which is the SST anomaly averaged over 5°N–5°S 170°W–120°W and is the most commonly used index to define El Niño (Trenberth, 1997). For pCO_2, we also show the linear trend. There are not enough nutrient data to detect a trend so they are not shown here. We calculated regression coefficients using the optimal interpolation results only where the interpolation square error ratios are less than 0.9 in order to avoid reduction of the signals (see Section 4.2.2). However, since the number of the interpolated results with low interpolation errors (square error ratios < 0.9) is limited especially for nutrients (see Section 4.2.2), the regression maps become noisy. Therefore, we also calculated regression coefficients from all interpolated results, which often underestimate the signal but are considered qualitatively reliable. Regression coefficients calculated from all interpolated results are sometimes opposite in sign to those calculated from the interpolated results with low estimation errors. It often happens where the observations are limited or the signals are weak. In that case, we consider the regression coefficients calculated from the interpolated results with low estimation errors are to be unreliable, and show just the sign of the regression coefficients calculated from all interpolated results.

3.6. Calculation of dissolved inorganic carbon

We calculated the value of total alkalinity (TA) from SSS and SST by using the simple empirical function, $TA = a + b\,(SSS - 35) + c\,(SSS - 35)^2 + d\,(SST - 20) + e\,(SST - 20)^2$, of Lee et al. (2006). The different coefficients "a" to "e" were specific to two regions in our analysis area: the equatorial upwelling region which was east of a line connecting [20°N, 75°W], [10°N, 110°W], [10°S, 110°W], and [20°S, 75°W], and the remaining tropical region. From pCO_2 gridded products and TA estimates, we calculated sea surface DIC concentration, using the CO2SYS program (Lewis and Wallace, 1998; van Heuven et al., 2009) with the dissociation constants of Lueker et al. (2000). We also calculated salinity normalized DIC to a constant salinity of 35 ($nDIC = 35 \times DIC/SSS$).

Overall uncertainties of TA estimate against the observation were reported as 8.1 μmol kg^{-1} (Lee et al., 2006), and these uncertainties affect the DIC estimation by about 6.5 μmol kg^{-1} when no uncertainty is

taken into account for other variables. Although a systematic bias in Lee's formulation was pointed out by Takatani et al. (2014), we used Lee's method in the present study because sea surface height data which Takatani's method requires are available only after 1993 (Kuragano and Kamachi, 2000) but the datasets used here date back to 1981. Using data after 1993, we confirmed the difference in TA value between Lee's method and Takatani's method is small in the tropical Pacific (Fig. 5 of Takatani et al. 2014), resulting in the same uncertainty for both methods (not shown).

3.7. Calculation of air-sea CO_2 fluxes

We calculated monthly air-sea CO_2 flux (F) values from the surface water pCO_2 (pCO_{2w}) values estimated in Sect. 3.4 by using the bulk formula:

$$F = kL(pCO_{2w} - pCO_{2a}), \quad (2)$$

where k is the gas transfer velocity and L is the solubility of CO_2. The solubility of CO_2 (L) was calculated as a function of SST and SSS (Weiss, 1974). We converted the interpolated NOAA marine boundary layer xCO_2 data (Sect. 2.2) to atmospheric pCO_2 (pCO_{2a}) by using monthly sea-level pressure data and the water-vapor saturation pressure calculated from monthly SST and SSS (Murray, 1967).

The gas transfer velocity k was calculated by using the formula of Sweeney et al. (2007):

$$k = 0.26\ (Sc/660)^{-0.5} <W^2>, \quad (3)$$

where Sc is the Schmidt number of CO_2 in seawater at a given SST, calculated according to Wanninkhof (2014), and $<W^2>$ is the monthly mean of the second moment of the NCEP2 6-hourly wind speed. The coefficient 0.26 is based on Sweeney et al. (2007) but optimized for NCEP2 winds following Takahashi et al. (2009). Although uncertainty in CO_2 flux by wind product is not small as discussed by Wanninkhof (2014) and Chiodi et al. (2019), our estimate of CO_2 outgassing integrated in the tropics (18°N–18°S, 120°E–70°W) is 0.40 ± 0.15 PgC yr^{-1} (mean ± standard error) which is similar to the estimate of 0.44 ± 0.14

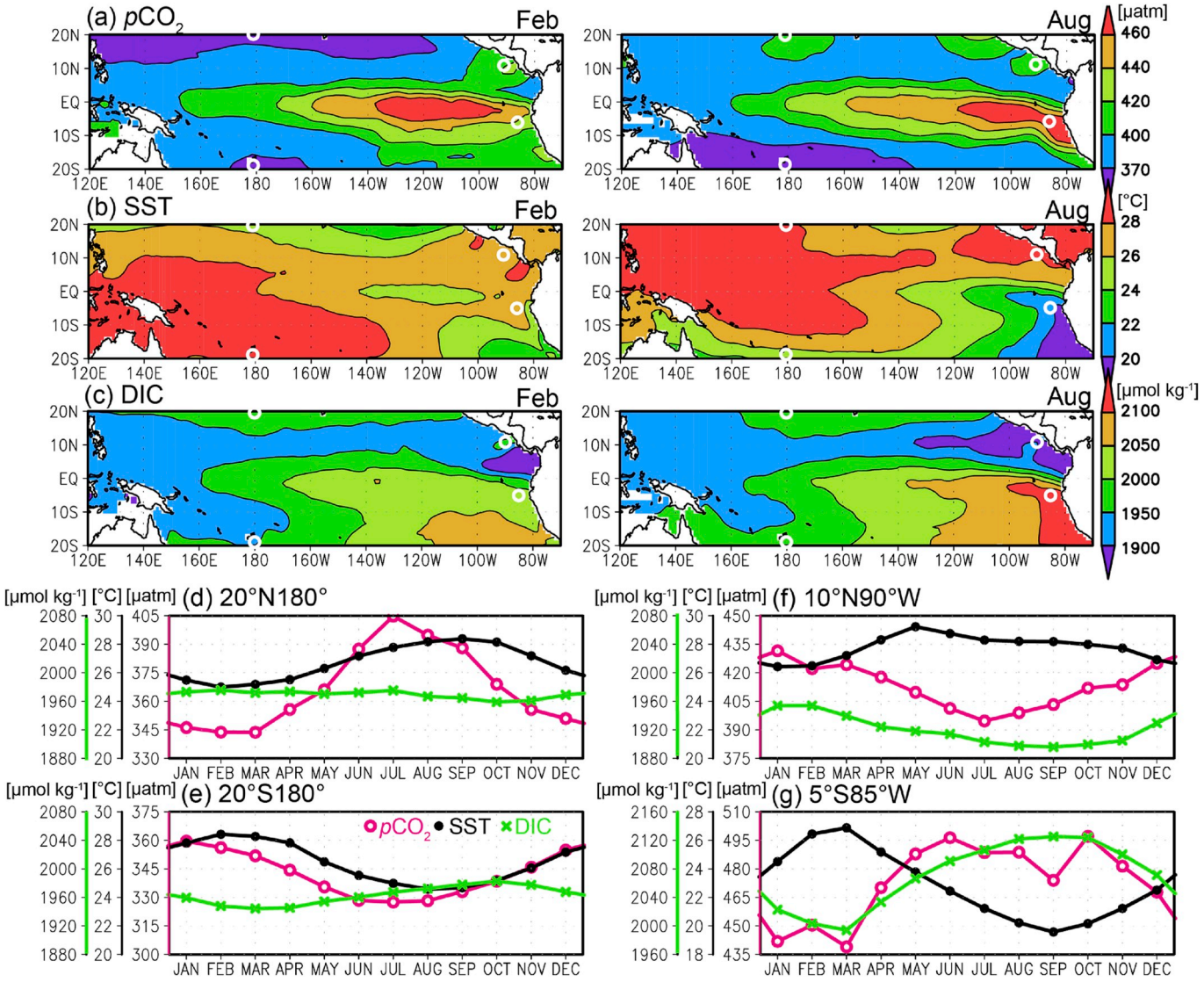

Fig. 3. (a–c) Long-term mean of seawater pCO_2 (a), SST (b) and DIC (c) in February (left) and August (right). (d−g) Seasonal variation of pCO_2 (magenta open circle), SST (black close circle) and DIC (green cross) at 20°N 180° (d), 20°S 180° (e), 10°N 90°W (f), and 5°S 85°W (g). White circles in a−c indicate the locations of d−g. (For interpretation of the references to colour in this figure legend, the reader is referred to the Web version of this article).

PgC yr $^{-1}$ by the synthesis study of Ishii et al. (2014).

4. Results

4.1. Seasonal variation

Surface seawater pCO_2 is high in the central to eastern equatorial region (Fig. 3a). From January to March when the coastal upwelling weakens (Nigam and Chao, 1996), high pCO_2 values along the South American coast decline (Fig. 3g). As a result, pCO_2 in February shows its maximum value from 140°W to 100°W, while in August the maximum is east of 120°W. Seasonal standard deviation in pCO_2, as well as SST and DIC, is large in the eastern tropics cold tongue region (EQ–20°S, east of 120°W), and small in the western tropics warm pool region (10°S–10°N, west of 140°W; Fig. 4a–c). Seasonal variation of pCO_2 is in-phase with seasonal variation of DIC and out-of-phase with seasonal variation of SST in the cold tongue regions; pCO_2 is high when and where DIC is high and SST is low (Fig. 3b, 3c and 3g). nDIC shows less north-south contrast in the eastern tropics, while the amplitude and phase of seasonal variation are quite similar to those of DIC (not shown there). These results imply that pCO_2 seasonal variation mainly depends on upwelling of subsurface cool, carbon-rich water.

Seawater pCO_2 has a local maximum off the coast of Central America (Fig. 3a). This pCO_2 local maximum region corresponds well with the DIC local maximum region and the SST local minimum region in February (Fig. 3b and c), when coastal upwelling is maximum (Clarke, 1988; Fiedler et al., 2002; Xie et al., 2005). Seasonal variation of pCO_2 is in-phase with seasonal variation of DIC (and nDIC) and out-of-phase with seasonal variation of SST in that region as in the case of the cold tongue region (Fig. 3f), which implies that pCO_2 seasonal variation mainly depends on upwelling of subsurface cool, carbon-rich water in this region as Walker Brown et al. (2015) showed in their regional study. In August, pCO_2 starts to increase with strengthening upwelling associated with the development of the Costa Rica Dome (Wyrtki, 1964; Fiedler et al., 2002). DIC increase would be diluted with the heavy rain in this season (Xie et al., 2005).

The seasonal standard deviation in seawater pCO_2 and SST is large in the off-equatorial region north of 10°N and south of 10°S (Fig. 4a and 4b). pCO_2 is at a minimum north of 10°N in the boreal winter, and south of 10°S in austral winter, both of which are in-phase with the seasonal variation in SST (Fig. 3a, 3b, 3d and 3e). On the other hand, the seasonal variation of DIC is weak there (Fig. 3c, 3d, 3e, and 4c). The magnitude of seasonal variation in SST is about 5 °C at 20°N 180° and 20°S 180° (Fig. 3d and e), which causes a pCO_2 variation of about 70 µatm (4.23% °C^{-1}; Takahashi et al., 1993). This value is consistent with the magnitude of the seasonal variation in pCO_2 there, although pCO_2 peaks a few months before SST, which can be ascribed to DIC (Fig. 3d and e). This suggests that pCO_2 seasonal variation mainly derives from thermodynamic effects in those regions.

Surface nutrients show high concentrations in the cold tongue region (EQ–20°S, east of 120°W; Fig. 5a–c). Similar to DIC, seasonal standard deviations of nutrients are large there, and small outside (Fig. 4c–f). Nutrient concentrations are high in austral winter, and the seasonal variations are in phase with DIC (Figs. 3g, 5a, 5b, 5c, and 5g). Maximum concentration off the coast of Central America in boreal winter is prominent only in phosphate, which is in phase with DIC (Fig. 3c, 3f, 5a, and 5f). In the subtropics (north of 10°N and south of 10°S), nutrient concentrations are low all year (Fig. 5a–e). Small seasonal standard deviations of nutrients in the subtropics are consistent with that of DIC (Fig. 4c–f). High concentrations of silicate in the northwestern region (EQ–20°N, 120°E–160°E) are related to several extreme values in the 1980s (Figs. 5c and S2), which could be measurement errors. Nitrate concentration in the eastern tropics is lower than expected from the Redfield ratio (N:P = 16:1); nitrate and phosphate concentrations are about 4–10 µmol kg^{-1} and 0.4–1.5 µmol kg^{-1}, respectively, which means the N:P ratio is about 7–10:1. The low N:P ratio could be attributed to denitrification in the subsurface hypoxic area, which is known as the oxygen minimum zone, although the N:P ratio of surface water is higher than the subsurface because of nitrogen fixation at surface (Deutsch et al., 2007; Meyer et al., 2017).

4.2. Interannual variability

4.2.1. Data covariance and signal-to-noise ratio

Fig. 6 shows the normalized covariance of surface seawater pCO_2 monthly anomalies. The normalized covariance averaged at each 1° latitudinal band decays with increasing distance (thin black lines in Fig. 6), although zonal covariance is noisy because most of the cruise

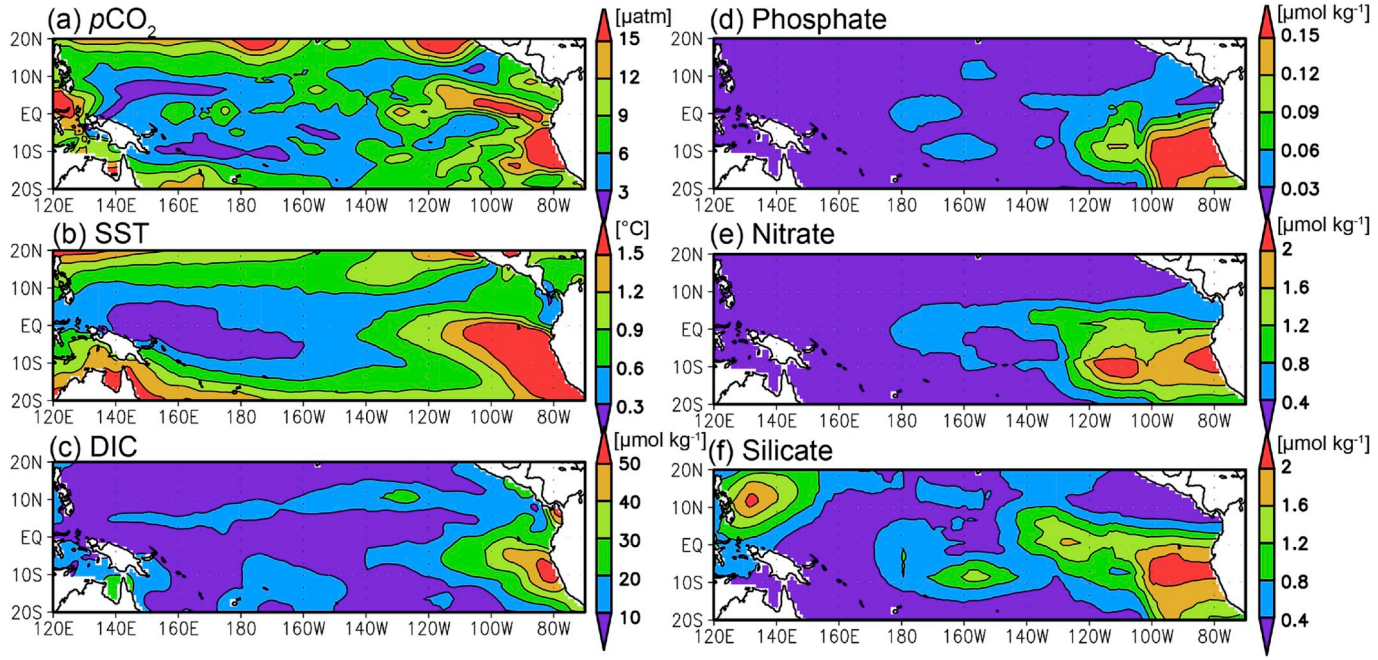

Fig. 4. Seasonal standard deviation of the long-term monthly means for (a) seawater pCO_2, (b) SST, (c) DIC, (d) phosphate, (e) nitrate, and (f) silicate.

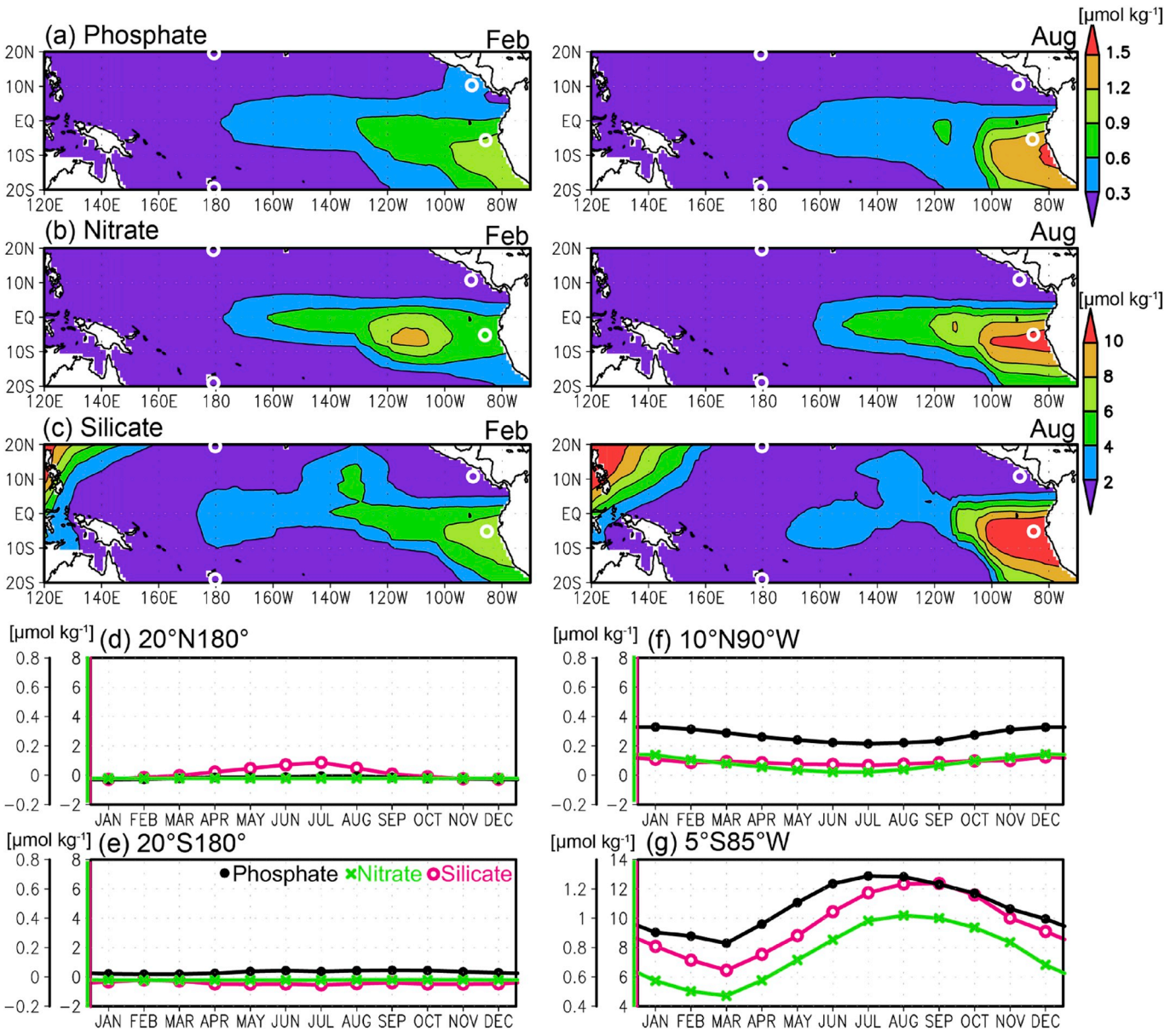

Fig. 5. (a–c) Long-term mean of phosphate (a), nitrate (b) and silicate (c) in February (left) and August (right). (d–g) Seasonal variation of phosphate (black close circle), nitrate (green cross) and silicate (magenta open circle) at 20°N 180° (d), 20°S 180° (e), 10°N 90°W (f), and 5°S 85°W (g). White circles in a–c indicate the locations of d–g. (For interpretation of the references to colour in this figure legend, the reader is referred to the Web version of this article).

routes are in the north-south direction. Covariance averaged over the analysis region shows an approximate exponential decay (thick magenta dashed lines in Fig. 6). Constant values of the best fitted exponential decay lines, i.e. e-folding scales, are 13° in the zonal direction, 6° in the meridional direction, and 2 months in the temporal direction (thick green lines in Fig. 6). Gaps of the normalized covariance between lag 0 and lag 1 average 0.8. The signal-to-noise ratio is therefore set to 4 [= 0.8/(1–0.8)]. We used the e-folding scales and signal-to-noise ratio obtained here for the optimal interpolation (see Section 3.4).

E-folding scales of nutrients were calculated to be 9° in the zonal direction, 6° in the meridional direction and 2 months in the temporal direction for phosphate, 7°, 6°, 1 month for nitrate, and 12°, 13°, 3 months for silicate. However, since pairs of nutrient data exist only in quite limited grids, covariance is quite scattered and an exponential decay fitting is not reasonable in many cases (not shown here). Therefore the e-folding scales and signal-to-noise ratio of pCO_2 were used for the optimal interpolation of nutrients.

4.2.2. *Distribution of the interpolation error*

Figs. 7 and 8 show normalized error variances of surface seawater pCO_2 and nitrate. For nutrients, we only present the error distribution of nitrate, but those for phosphate and silicate are quite similar. Interpolation error is small when and where there are observations nearby.

For pCO_2, the errors are small only along the 137°E line in early 1980s, but also along several lines after that (Fig. 7a–d). Three SOO routes and six pCO_2 mooring points can be seen in 2011 (Fig. 7d). Along the equator, the errors are small in almost all areas since the late 1980s, but the area where the errors are large appears again after the 2010s due to a reduction in regular ship visits (Fig. 7e).

For nutrients, the error is small in the western region (west of 180°) due to frequent hydrographic observations since the early 1980s and SOO samplings after 2006 (Fig. 8). The error is large in the central to eastern region except for in the early 1990s when there were World Ocean Circulation Experiment (WOCE) and Joint Global Ocean Flux Study (JGOFS) observations.

Optimal interpolation results with large square error ratios tend to

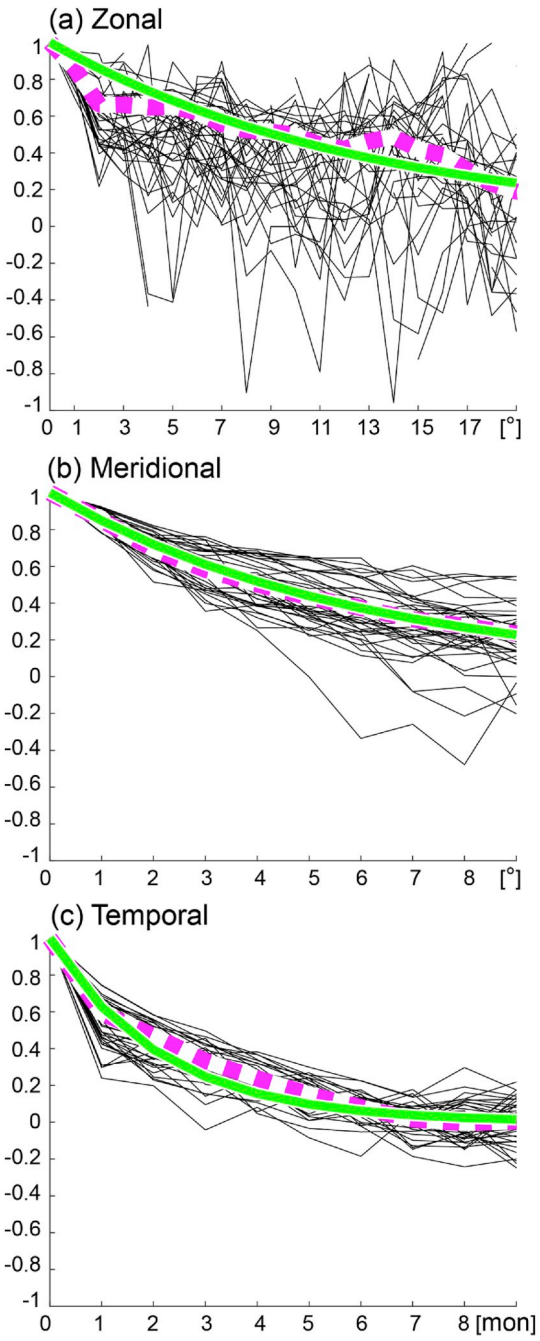

Fig. 6. Normalized covariance of the detrended seawater pCO_2 anomaly averaged at each 1° latitudinal band (thin black lines) and averaged over the analysis region (thick magenta dashed line) for (a) zonal, (b) meridional and (c) temporal dimensions. Thick green line denotes the best fit of exponential decay. (For interpretation of the references to colour in this figure legend, the reader is referred to the Web version of this article.)

agree with the monthly climatology (Hosoda et al., 2008). We found the anomalies from the monthly climatology have small magnitudes when the square error ratios are more than approximately 0.9. This means that the optimal interpolation results with square error ratios >0.9 tend to underestimate the interannual variation. For pCO_2, each $1° \times 1°$ grid box in most of the tropical Pacific contains more than 30 data points where the interpolation square error ratios are less than 0.9 during the period from 1981 to 2015 (Fig. 9a). For nutrients, there are many grid cells which contain fewer than 10 data points in the central to eastern region, and the grid cells which contain more than 30 data points are only in the western tropics and in the coastal regions of Central and South America (Fig. 9b–c).

4.2.3. Spatio-temporal variability

Interannual standard deviations of surface seawater pCO_2 and DIC anomalies are large along the equator, while standard deviations of nutrients are large in the eastern tropics (Fig. 10). The spatial patterns of the pCO_2 and DIC interannual standard deviations are different from that of the seasonal standard deviations, while spatial patterns of the nutrient interannual standard deviations are similar to those of the seasonal standard deviations (see Fig. 4). The pCO_2 and DIC interannual standard deviations along the equator are larger than the seasonal standard deviations, while those in the cold tongue region (EQ–20°S, east of 120°W) are comparable.

Seawater pCO_2 decreases in almost all areas within the analysis area (20°N–20°S) when El Niño occurs; the significant negative anomalies spread over 5°N–5°S, and the pCO_2 decreases are the largest at the equator (Fig. 11a). Time series of pCO_2 anomalies along the equator clearly show the increase during La Niña and the decrease during El Niño between 147°E and 110°W (Fig. S1). The DIC signal shows a similar pattern to the pCO_2 signal, but the positive anomalies in the western off-equatorial region are more prominent in DIC than in pCO_2. Also, the area with significant negative anomalies is larger in DIC than in pCO_2 (Fig. 11b). This is because the pCO_2 variation along with DIC variation in El Niño is partly compensated by temperature variation. A rise of 0.5 °C in SST, which is roughly the SST El Niño signal in the eastern equatorial Pacific (Fig. 11g), causes a pCO_2 rise of about 8 µatm (4% $°C^{-1}$; Takahashi et al., 1993). The pCO_2 signal is about –10 µatm in the eastern equatorial Pacific (Fig. 11a), which means the signal is weakened by half by the temperature effect. West of 180°, the SSS change associated with ENSO also affects DIC. During El Niño, SSS is low along the equator and high in the off-equatorial region in the western Pacific as shown by Delcroix (1998). This causes a decrease and increase in DIC, respectively. The nDIC signal in the western tropics is weaker than the DIC signal (not shown).

The long term seawater pCO_2 trend is positive in all regions, and the area average is 1.84 ± 0.07 µatm yr^{-1} (mean ± standard error; Fig. 12a), which is slightly larger than the area average of atmospheric pCO_2 trend (1.66 ± 0.01 µatm yr^{-1}). The pCO_2 trend is not uniform in space, and is > 2 µatm yr^{-1} in most places in the eastern tropics (160°W–90°W) and along the equator.

The long-term DIC trend is also positive in all regions (Fig. 12b). DIC trends, like pCO_2 trends, tend to be larger along the equator than off-equator, and larger in the eastern tropics than in the western tropics. The DIC trend averaged over the analysis domain is 1.4 ± 0.1 µmol kg^{-1} yr^{-1}. The nDIC trend in the western equatorial region (5°N–5°S, 144°E–160°W) is 1.0 ± 0.1 µmol kg^{-1}.

Nutrient concentrations tend to be low in the central to eastern equatorial region (10°N–10°S, 180°–80°W) when El Niño occurs (Fig. 11d–f), which aligns with the DIC variation (Fig. 11b). The time series of phosphate and nitrate anomalies at EQ 165°E showed an increase during La Niña and a decrease during El Niño (Fig. S2), although the ENSO signals in other regions are unclear. Where data coverage is good in the west, the ENSO signal is weak; however, data are sparse in the east where we expect a stronger ENSO signal. The magnitudes of the phosphate and nitrate signals are smaller than expected from the Redfield ratio with the DIC signal, which would be due to an inadequate number of nutrient observations. We confirmed that the DIC signal is similar to the nDIC signal in the eastern equatorial region.

4.2.4. Interannual variability of winds and CO_2 fluxes

During El Niño, easterly winds weaken in the central to western tropics (Fig. 11h), which leads to weak upwelling of the DIC-rich subsurface water as shown in several equatorial locations (Feely et al., 2002, 2006; Ishii et al., 2009; Sutton et al., 2014). The contribution of atmospheric pCO_2 variability to the air-sea CO_2 flux variability is

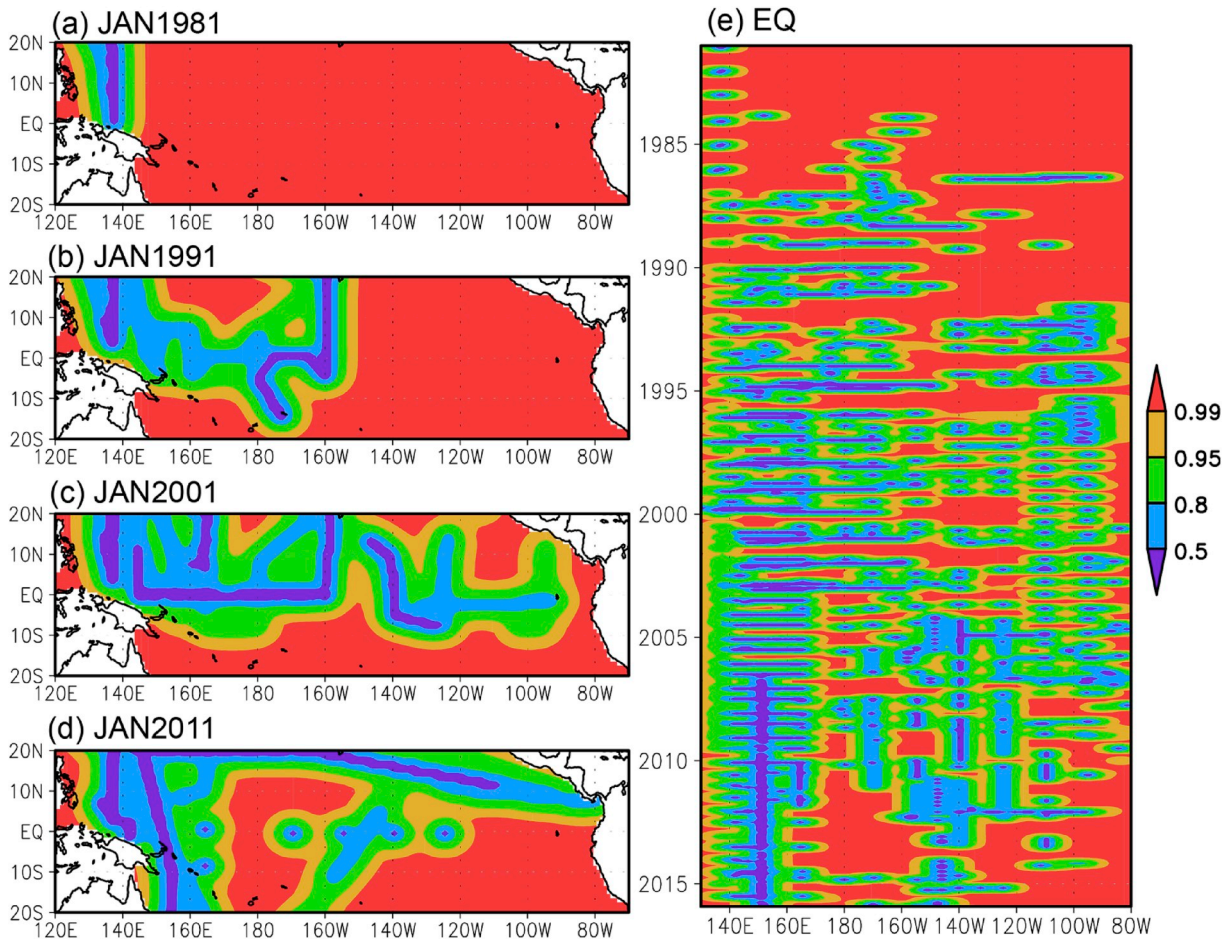

Fig. 7. Normalized error variance of seawater pCO_2 anomaly in January (a) 1981, (b) 1991, (c) 2001, (d) 2011, and (e) along the equator (2°N–2°S) from January 1981 to December 2015.

insignificant and much smaller than that of seawater pCO_2, as Feely et al. (2002) and Ishii et al. (2009) showed along the equator for several El Niño. Therefore ΔpCO_2 is reduced in parallel with seawater pCO_2 (not shown).

During El Niño, CO_2 outgassing is suppressed from 160°E to 140°W on the equator, but the CO_2 flux change is small in the other region (Fig. 11f). That is, the CO_2 flux averaged over the tropical Pacific is suppressed during El Niño. ΔpCO_2 is reduced in the whole equatorial region as mentioned above, while the winds weaken from 160°E to 140°W, and strengthen west of 160°E and east of 140°W (Fig. 11i). Therefore, the suppression of CO_2 outgassing from 160°E to 140°W is due to the reduction of ΔpCO_2 and weak winds, while the weak CO_2 flux change west of 160°E and east of 140°W at the equator is due to the opposing effects of ΔpCO_2 reduction and strong winds.

The trend in CO_2 outgassing is positive (i.e., CO_2 outgassing is strengthened) in boxes defined by EQ–15°S, 140°W–90°W, and 2°N–5°S, 170°E–160°W, while it is negative around EQ, 150°W, 10°N, 140°E, and 20°S 160°E (Fig. 12c). The strengthened CO_2 outgassing is related to the positive trend of ΔpCO_2 (Fig. 12d), and the weakened CO_2 outgassing is related to the weakened surface wind (Fig. 12g). Since it is not uniform in space, the trend of CO_2 outgassing averaged over the entire tropical Pacific region is much less than the uncertainty (4 ± 11 PgC yr^{-1} yr^{-1}).

In our analysis period (1981–2015), SST cooled in the central to eastern tropics (Fig. 12e), and zonal winds strengthened (Fig. 12f), which is similar to the negative Pacific Decadal Oscillation (PDO) pattern (Mantua et al., 1997). Indeed, the PDO index shows a weak negative trend during the period from 1981 to 2015 (not shown). The expected global warming trend would be for SST to increase, especially in the eastern tropics, and the trade winds to be weakened (Tokinaga et al., 2011), which is the opposite to the trend from 1981 to 2015 presented here. Therefore, the spatial pattern of the long-term trend in pCO_2 obtained here is likely not associated with global warming but with the PDO. To detect the spatial pattern of pCO_2 and CO_2 flux associated with global warming, pCO_2 observations over a longer period are needed, to reduce the imprint of the PDO on the time series.

5. Discussion

5.1. Comparison of spatial and temporal variability with previous studies

DIC-dependent pCO_2 seasonal variation in the eastern tropics cold tongue region (EQ–20°S, east of 120°W) in our study (see Section 4.1) is consistent with the modelling result of Wang et al. (2006). However, the negative correlation between SST and pCO_2 in our study is not consistent with other modelling studies (Jiang and Chai, 2006; Wang et al., 2015), yet is in line with observation-based results (Cosca et al., 2003; Feely et al., 2006).

The seawater pCO_2 decrease along the equator during El Niño (see Section 4.2.3) is consistent with many other studies (Feely et al., 1999, 2002, 2006; Ishii et al., 2009, 2014), while we find the spatial breadth of the negative signal (Fig. 11a) separated from the seasonal variation whose standard deviations are comparable with the ENSO signal in some areas (see Fig. 4a).

The seawater pCO_2 trend estimated in Section 4.2.3 is consistent with the previous time series analysis and area-averaged estimates as follows.

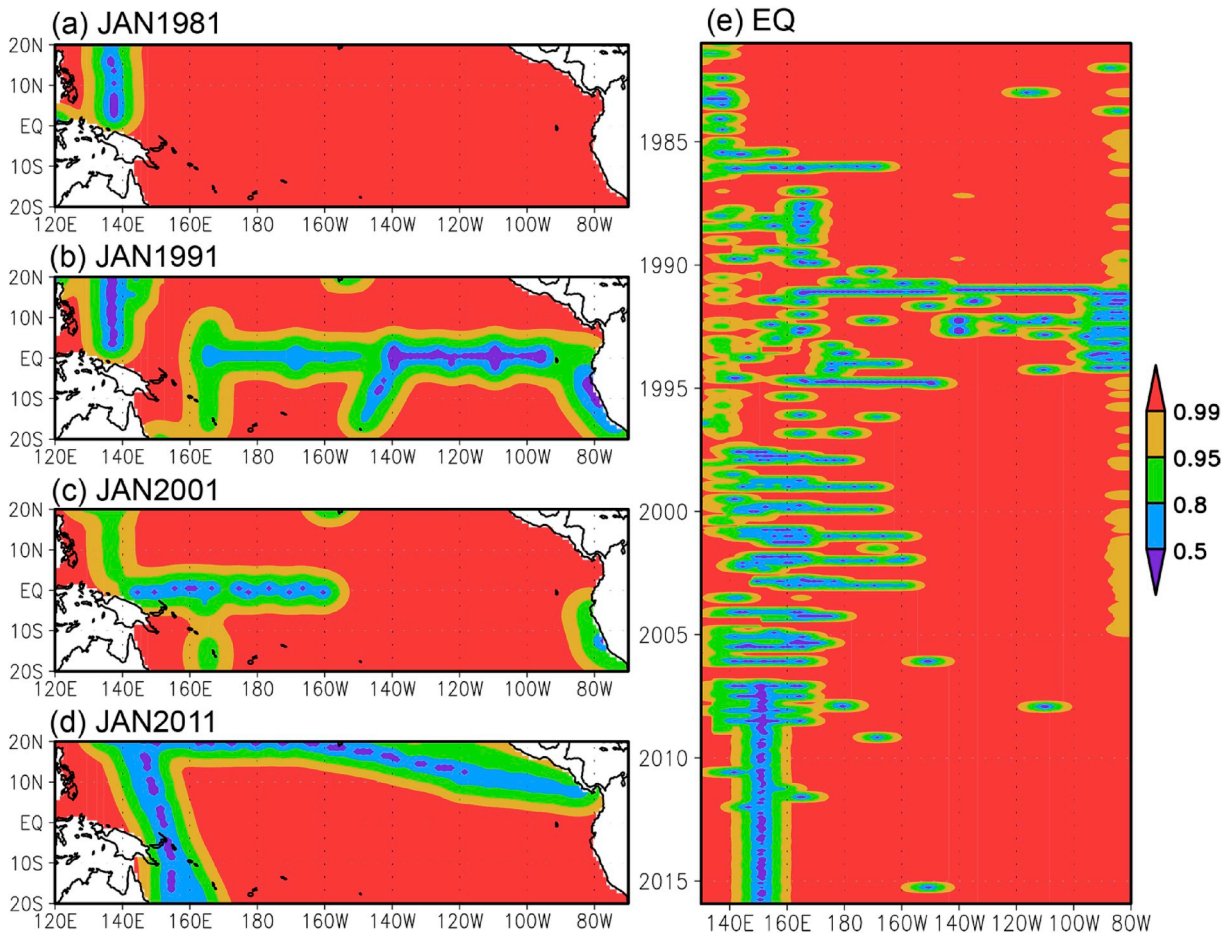

Fig. 8. Normalized error variance of nitrate anomaly in January (a) 1981, (b) 1991, (c) 2001, (d) 2011, and (e) along the equator (2°N–2°S) from January 1981 to December 2015.

Magnitudes of the trend at the central to eastern equator (170°W–125°W) in our study are 1.6–3.2 μatm yr^{-1} and quite similar to those reported by Sutton et al. (2014; 1.6–3.3 μatm/yr at 170°W, 155°W, 140°W, and 125°W for 1997–2011), although they are not exactly consistent on a point-by-point basis. Our trend in the western equatorial region (5°N–5°S, 144°E–160°W) is 1.83 ± 0.08 μatm yr^{-1}, which is larger than the estimate of Ishii et al. (2009; 1.4–1.6 μatm yr^{-1}) due to the different time periods used in each study. Analyzing our product for the 1985–2004 period assessed by Ishii et al. (2009), we find a similar trend of 1.43 ± 0.08 μatm yr^{-1}. nDIC trend in the western equatorial region is consistent with the estimate of Ishii et al. (2009; 0.8–1.3 μmol kg^{-1} yr^{-1}).

The suppressed CO_2 outgassing averaged over the tropical Pacific during El Niño has been found in many previous studies (Feely et al., 1995, 1997, 1999, 2002, 2006; Takahashi et al., 2003; Ishii et al., 2009; Sutton et al., 2014), but our results clarify that the signal is not uniform and shows large variability in space (see Section 4.2.4). Previous studies also showed contrasting ENSO signals between eastern and western tropics (Patra et al., 2005; Ishii et al., 2014; Rödenbeck et al., 2015), but the area of the suppression of CO_2 outgassing we presented is different to the areas presented in previous studies.

Although strengthened CO_2 outgassing in the eastern tropics in recent years is consistent with the synthesis study by Rödenbeck et al. (2015), the positive trend area is not identical to the biome they used. Almost zero trend of CO_2 outgassing averaged over the entire tropical Pacific region is consistent with the synthesis study by Ishii et al. (2014). Decadal modulations of equatorial averaged pCO_2 and CO_2 flux trends have been reported by other studies (Takahashi et al., 2003; Feely et al., 2006; Ishii et al., 2014), while we further characterize the spatial distribution.

Our estimates of the e-folding scales of seawater pCO_2 (Section 4.2.1) are larger and longer but in the same order with those estimates by Gasparin et al. (2015) in which e-folding scales of steric height were about 4°–9° in space, and 15 days in time. It is noted that e-folding scales in this study are larger than those presented by Jones et al. (2012; 400 ± 250 km) since we focus on the interannual variability while Jones et al. (2012) performed their analysis on the pCO_2 distribution itself including long-term mean states.

5.2. Comparison with other gridded products

5.2.1. Seawater pCO_2

Fig. S3 shows time series at several points and spatial distribution in February 2012 in other seawater pCO_2 gridded products. All pCO_2 values from the gridded products follow well the pCO_2 values from measurements archived in SOCATv5. The root-mean-square (RMS) differences between pCO_2 values from gridded products and pCO_2 measured values in SOCATv5 are 0.68, 1.68, and 2.60 μatm, for our product, ETH_SOM-FFN, and JMA_MLR respectively. RMS differences among the pCO_2 values from each gridded product are 14.7–17.8 μatm. The pCO_2 values from gridded products agree with measured values, but the gridded values include large uncertainties when they are away from the observations in time and space.

Long-term monthly mean fields for ETH_SOM-FFN and JMA_MLR are generally similar with our results (Figs. S4a and S4b, compared to Fig. 3a). pCO_2 is high in the central to eastern equatorial region, and

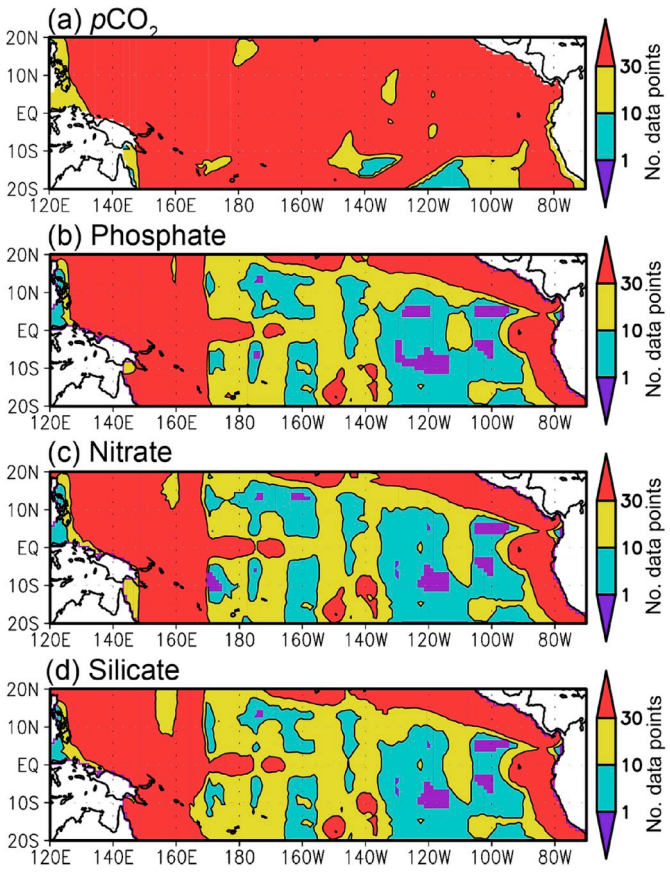

Fig. 9. Number of data points with low estimation errors (square error ratios < 0.9) of (a) seawater pCO_2, (b) phosphate, (c) nitrate, and (d) silicate.

shows a local maximum off the coast of Central America. A slight discontinuity can be seen along 10°S and 15°S in JMA_MLR, which is the boundary of their biome (Fig. S4b). Seasonal cycles of JMA_MLR are consistent with our data in terms of both the phases and the amplitudes in every region (Figs. S4c–S4f). On the other hand, the seasonal cycle off the coast of Central America is different in ETH_SOM-FFN; it shows a much higher value (>450 µatm) from February to May than the other two products (Fig. S4e). High pCO_2 values sometimes appeared in November to February but not in March to May in SOCATv5, as pointed out by Walker Brown et al. (2015). This suggests the ETH_SOM-FFN may not adequately represent this local feature due to placement within the same biome as the subtropical South Atlantic (Landschützer et al., 2014), even though pCO_2-SST relationships in these two regions are opposite (Takahashi et al., 2002).

Seawater pCO_2 variations related to ENSO are similar in the gridded products; pCO_2 is low in the equatorial region when El Niño occurs (Figs. 11a and S5a). In JMA_MLR, slight discontinuity can be seen along 10°S, and a positive pCO_2 signal south of 10°S is significant. Both products show that the long term pCO_2 trends are larger in the central to eastern equatorial region than in the other region (Fig. S5b), which is consistent with our product (Fig. 12a). The long-term pCO_2 trends across the entire tropical Pacific region are 1.79 ± 0.05 µatm yr^{-1} in ETH_SOM-FFN, and 1.86 ± 0.04 µatm yr^{-1} in JMA_MLR, both of which are consistent with the area-averaged trend in our products (1.84 ± 0.07 µatm yr^{-1}).

Other studies on pCO_2 variability in the tropical Pacific used correlations between SST and pCO_2 to estimate pCO_2 distribution (e.g. Cosca et al., 2003; Feely et al., 2006). The SST-pCO_2 relation is clear for the whole equatorial region at interannual time scales, but just in the upwelling region for seasonal variation (see Section 4.3). This introduces uncertainty of the estimated pCO_2 as Wang et al. (2015) implied through their model. Consequently, although similar spatio-temporal variability of pCO_2 is seen (see Section 5.1), they could include several artificial signals as shown in this section.

Although our product does not show the meaningful signals in data sparse regions and time periods, uncertainty of the signals are illustrated by the interpolation errors. As a result of these estimated uncertainties,

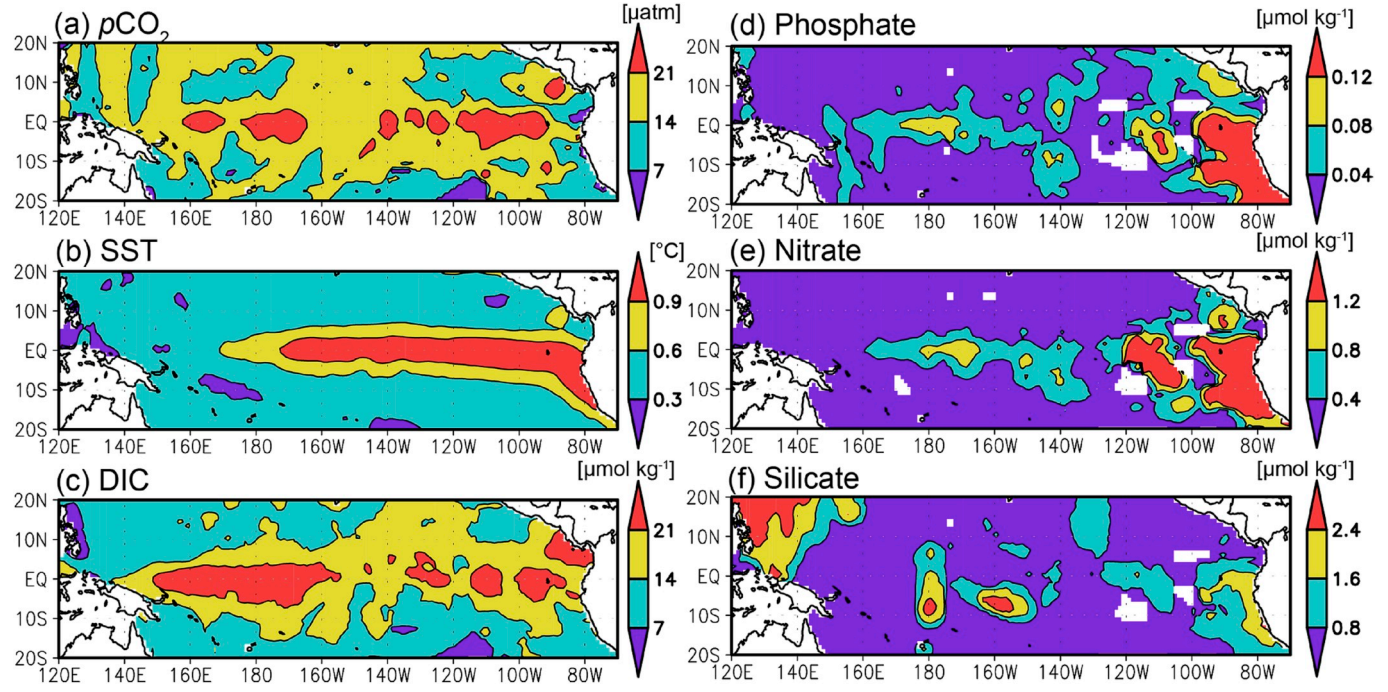

Fig. 10. Standard deviation of (a) seawater pCO_2, (b) SST, (c) DIC, (d) phosphate, (e) nitrate, and (f) silicate interannual variability calculated from the optimal interpolation results with low estimation errors (square error ratios < 0.9).

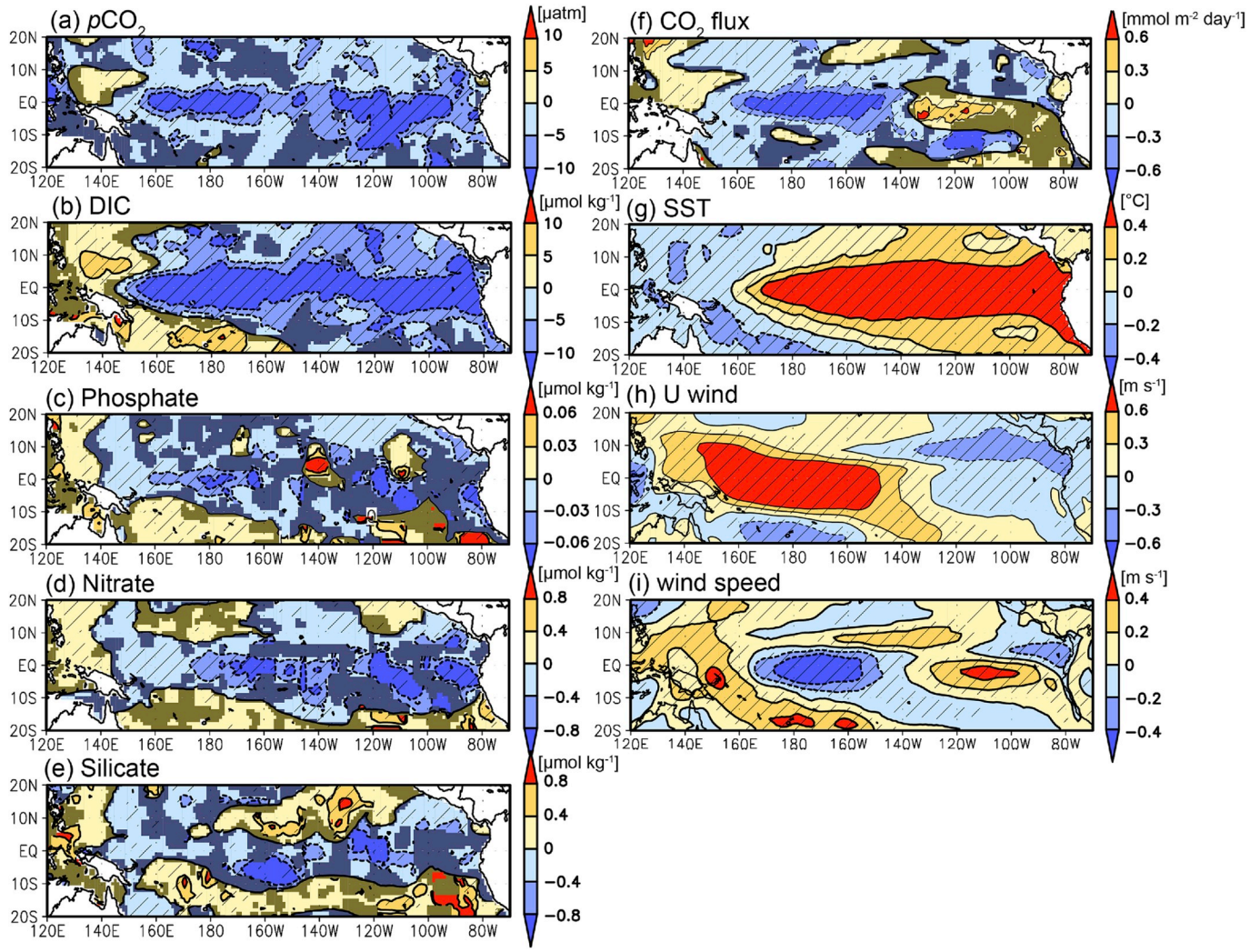

Fig. 11. Regression maps of (a) seawater pCO_2, (b) DIC, (c) phosphate, (d) nitrate, and (e) silicate, (f) air-sea CO_2 flux, (g) SST, (h) surface zonal wind, and (i) surface wind speed onto the Niño 3.4 index. Regression coefficients in a−f is calculated from the optimal interpolation results with low estimation errors (square error ratios < 0.9). Dark red (blue) in a−f shows positive (negative) regression coefficient calculated from all optimal interpolation results (see text). Hatched areas with diagonal lines indicate regression coefficients significant at $p < 0.05$. (For interpretation of the references to colour in this figure legend, the reader is referred to the Web version of this article).

we could assess the robustness of the previous results with our product.

5.2.2. *Nutrients*

We examined seasonal variability in the WOA13 climatology (Fig. S6). Spatial distributions of WOA13 are generally similar to those of our data, but WOA13 shows the unnatural large-scale meander of contours and local maxima along meridional lines (Figs. S6a–c). For example, the high concentration of silicate along 180° appears inconsistent in time and among nutrient components. Unrealistic high concentration of silicate near the Philippines can be seen in WOA13 (Fig. S6c) as in our data (Fig. 4c). Seasonal cycles of WOA13 are vaguely similar to our products, but they are quite noisy (Figs. S6d–g). It should be noted that our product includes interannual variability as discussed in Section 4.2, while WOA13 does not.

6. Concluding remarks

Through synthesis of surface seawater pCO_2 and surface nutrient observations, we assessed their variability in the tropical Pacific. We separately characterized basin-scale distributions of the seasonal and interannual variability of pCO_2 and nutrients based on the gridded products which we developed using interpolation of measured values without any relationships with other variables. We also quantified the spatial distribution of the long-term pCO_2 trend beyond the area-averaged trend published previously. Furthermore, the spatial patterns of the ENSO signal of nutrients were firstly presented. Our results will be useful for validation of ocean biogeochemical and Earth system models.

Surface seawater pCO_2 observations can characterize pCO_2 and CO_2 flux interannual variability, but the recent decrease in the observation density and frequency in the central to eastern tropics is of great concern. Our estimates of e-folding scale suggest that underway pCO_2 observations by twice annual servicing of the TAO array along the latitudinal transects in every 15° of longitude are suitable to capture the interannual spatial variability of pCO_2, while more frequent observations by the SOO and moorings are better able to capture the temporal variation. Furthermore, since the magnitudes of long-term trends in a limited analysis period are affected by interannual variability such as the PDO, sustained monitoring is needed to identify the spatial pattern associated with longer term climate change.

Nutrient observations are sparse in the central to eastern tropics, and are often not sufficient to quantify the interannual spatio-temporal variability. Installing nitrate sensors as part of underway observing systems and increasing the coverage of biogeochemical floats are promising ways to increase surface nutrient data.

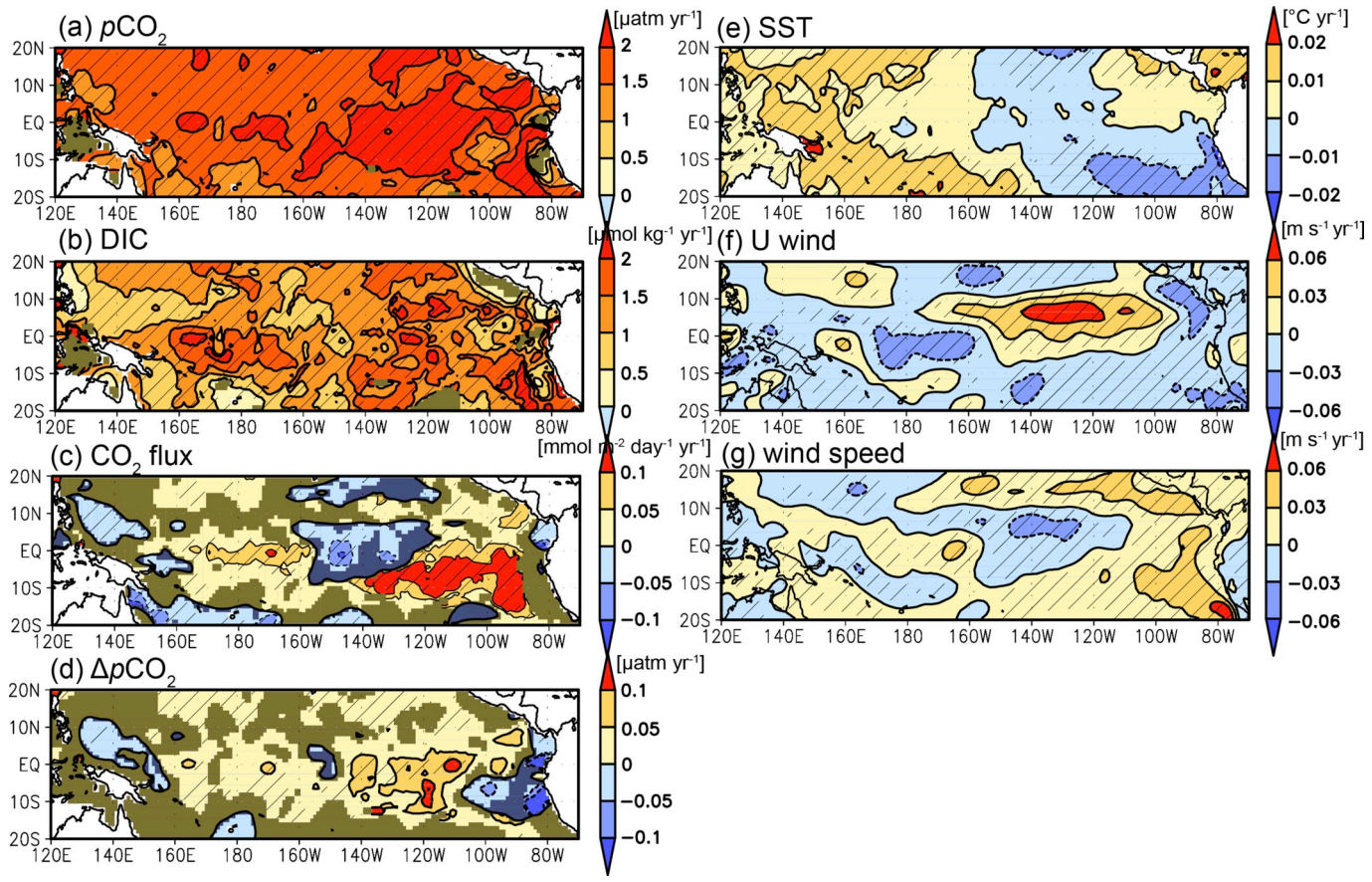

Fig. 12. Liner trend from 1981 to 2015 of (a) seawater pCO_2, (b) DIC, (c) CO_2 flux, (d) ΔpCO_2, (e) SST, (f) surface zonal wind, and (g) surface wind speed. Liner trend in a–d shown is calculated from the optimal interpolation results with low estimation errors (square error ratios < 0.9). Dark red (blue) in a–d shows positive (negative) regression coefficient calculated from all optimal interpolation results (see text). Hatched areas with diagonal lines indicate regression coefficients significant at $p < 0.05$. (For interpretation of the references to colour in this figure legend, the reader is referred to the Web version of this article).

We found questionable silicate concentration data in EQ-20°N, 120°E–160°E in the 1980s. They cannot be eliminated by simple statistical quality controls as a consequence of their large number. Close attention to data quality is needed especially for older data.

Although the gridded pCO_2 products using empirical relationships have seemingly realistic values, we have to pay attention for several artificial signals which probably stem from the estimation methods. On the other hand, our products can be used to assess the pCO_2 variability if future users remove the values associated with large interpolation errors. Furthermore, our product shows the data deficit areas clearly, which would be useful for future observation planning.

Data synthesis is as important as the observation itself to clarify the variability, especially at large spatial scales and on long temporal scales. Data archiving and quality control efforts such as SOCAT, GLODAP, and WOD should continue to be encouraged.

Declaration of competing interest

The authors declare that they have no known competing financial interests or personal relationships that could have appeared to influence the work reported in this paper.

Acknowledgements

We thank the many researchers and funding agencies responsible for the collection of data and quality control for their contributions to SOCAT, GLODAP, WOD, and NIES SOO observations. Among SOCAT pCO_2 data we used, 25% of cruises were provided by Yukihiro Nojiri, 15% by Richard Feely and 14% by Shu Saito. We are grateful for the use of the CO2SYS program obtained from the Ocean Carbon Data System of NOAA National Centers for Environmental Information (https://www.nodc.noaa.gov/ocads/oceans/CO2SYS/co2rprt.html). Comments from the editor and anonymous reviewers were helpful in improving the manuscript. This work was financially supported by JSPS KAKENHI Grant Number JP 18H04129, and in part by the Global Environmental Research Coordination System, from the Ministry of the Environment, Japan (E1751). AJS is supported by the Office of Oceanic and Atmospheric Research of the National Oceanic and Atmospheric Administration, U.S. Department of Commerce, including resources from the Ocean Observing and Monitoring Division. This is PMEL contribution #4859.

Appendix A. Supplementary data

Supplementary data to this article can be found online at https://doi.org/10.1016/j.dsr2.2019.104680.

References

Alaka, M.A., Elvander, R.C., 1972. Optimum interpolation from observations of mixed quality. Mon. Weather Rev. 100, 612–624. https://doi.org/10.1175/1520-0493(1972)100<0612:OIFOOM>2.3.CO;2.

Bakker, D.C.E., et al., 2016. A multi-decade record of high-quality fCO_2 data in version 3 of the Surface Ocean CO2 Atlas (SOCAT). Earth Syst. Sci. Data 8, 383–413. https://doi.org/10.5194/essd-8-383-2016.

Boyer, T.P., Antonov, J.I., Baranova, O.K., Coleman, C., Garcia, H.E., Grodsky, A., Johnson, D.R., Locarnini, R.A., Mishonov, A.V., O'Brien, T.D., Paver, C.R., Reagan, J. R., Seidov, D., Smolyar, I.V., Zweng, M.M., 2013. World Ocean Database 2013.

Sydney Levitus. In: Alexey Mishonov, Technical, vol. 72. NOAA Atlas NESDIS, p. 209.
Chavez, F.P., Barber, R.T., 1987. An estimate of new production in the equatorial Pacific. Deep-Sea Res. 34, 1229–1243. https://doi.org/10.1016/0198-0149(87)90073-2.
Chiodi, A.M., Dunne, J.P., Harrison, D.E., 2019. Estimating air-sea carbon flux uncertainty over the tropical Pacific: importance of winds and wind analysis uncertainty. Glob. Biogeochem. Cycles 33, 370–390. https://doi.org/10.1029/2018GB006047.
Clarke, O., 1988. Employment adjustment: an international perspective. Lab. Trav. 2, 3–29. https://doi.org/10.1111/j.1467-9914.1988.tb00126.x.
Conway, T.J., Tans, P.P., Waterman, L.S., Thoning, K.W., Kitzis, D.R., Masarie, K.A., Zhang, N., 1994. Evidence for interannual variability of the carbon cycle from the NOAA/CMDL global air sampling network. J. Geophys. Res. 99, 22831–22855. https://doi.org/10.1029/94JD01951.
Cosca, C.E., Feely, R.A., Boutin, J., Etcheto, J., McPhaden, M.J., Chavez, F.P., Strutton, P. G., 2003. Seasonal and interannual CO_2 fluxes for the central and eastern equatorial Pacific Ocean as determined from fCO_2-SST relationships. J. Geophys. Res. 108 (C8), 3278. https://doi.org/10.1029/2000JC000677, 2003.
Delcroix, T., 1998. Observed surface oceanic and atmospheric variability in the tropical Pacific at seasonal and ENSO timescales: A tentative overview. J. Geophys. Res. 103, 18611–18633. https://doi.org/10.1029/98JC00814.
Deutsch, C., Sarmiento, J.L., Sigman, D.M., Gruber, N., Dunne, J.P., 2007. Spatial coupling of nitrogen inputs and losses in the ocean. Nature 445, 163–167. https://doi.org/10.1038/nature05392.
Echevin, V., Aumont, O., Ledesma, J., Flores, G., 2008. The seasonal cycle of surface chlorophyll in the Peruvian upwelling system: a modelling study. Prog. Oceanogr. 79, 167–176. https://doi.org/10.1016/j.pocean.2008.10.026.
Feely, R.A., Gammon, R.H., Taft, B.A., Pullen, P.E., Waterman, L.S., Conway, T.J., Gendron, J.F., Wisegarver, D.P., 1987. Distribution of chemical tracers in the eastern equatorial Pacific during and after the 1982–1983 El Niño/Southern Oscillation event. J. Geophys. Res. 92, 6545–6558. https://doi.org/10.1029/JC092iC06p06545.
Feely, R.A., Wanninkhof, R., Cosca, C.E., Murphy, P.P., Lamb, M.F., Steckley, M.D., 1995. CO_2 distributions in the equatorial Pacific during the 1991–1992 ENSO event. Deep Sea Res. Part II 42, 365–386. https://doi.org/10.1016/0967-0645(95)00027-N.
Feely, R.A., Wanninkhof, R., Goyet, C., Archer, D.E., Takahashi, T., 1997. Variability of CO_2 distributions and sea-air fluxes in the central and eastern equatorial Pacific during the 1991–1994 El Niño. Deep Sea Res. Part II 44, 1851–1867. https://doi.org/10.1016/S0967-0645(97)00061-1.
Feely, R.A., Wanninkhof, R., Takahashi, T., Tans, P., 1999. Influence of El Niño on the equatorial Pacific contribution of atmospheric CO2 accumulation. Nature 398, 597–601. https://doi.org/10.1038/19273.
Feely, R.A., Boutin, J., Cosca, C.E., Dandonneau, Y., Etcheto, J., Inoue, H.Y., Ishii, M., Le Quere, C., Mackey, D., McPhaden, M., Metzl, N., Poisson, A., Wanninkhof, R., 2002. Seasonal and interannual variability of CO_2 in the equatorial Pacific. Deep Sea Res. Part II 49, 2443–2469. https://doi.org/10.1016/S0967-0645(02)00044-9.
Feely, R.A., Takahashi, T., Wanninkhof, R., McPhaden, M.J., Cosca, C.E., Sutherland, S. C., Carr, M.-E., 2006. Decadal variability of the air-sea CO2 fluxes in the equatorial Pacific Ocean. J. Geophys. Res. 111, C08S90. https://doi.org/10.1029/2005JC003129.
Fiedler, P.C., 2002. The annual cycle and biological effects of the Costa Rica Dome. Deep-Sea Res. I 49, 321–338.
Garcia, H.E., Locarnini, R.A., Boyer, T.P., Antonov, J.I., Baranova, O.K., Zweng, M.M., Reagan, J.R., Johnson, D.R., 2014. In: Levitus, S., Mishonov Technical, A. (Eds.), World Ocean Atlas 2013, Volume 4: Dissolved Inorganic Nutrients (Phosphate, Nitrate, Silicate), NOAA Atlas NESDIS, vol. 76, p. 25.
Gasparin, F., Roemmich, D., Gilson, J., Cornuelle, B., 2015. Assessment of the upper-ocean observing system in the equatorial Pacific: the role of Argo in resolving intraseasonal to interannual variability. J. Atmos. Ocean. Technol. 32, 1668–1688. https://doi.org/10.1175/JTECH-D-14-00218.1.
Good, S.A., Martin, M.J., Rayner, N.A., 2013. EN4: quality controlled ocean temperature and salinity profiles and monthly objective analyses with uncertainty estimates. J. Geophys. Res. 118, 6704–6716. https://doi.org/10.1002/2013JC009067.
Horel, J.D., 1982. On the annual cycle of the tropical Pacific atmosphere and ocean. Mon. Weather Rev. 110, 1863–1878. https://doi.org/10.1175/1520-0493(1982)110<1863:OTACOT>2.0.CO;2.
Hosoda, S., Ohira, T., Nakamura, T., 2008. A monthly mean dataset of global oceanic temperature and salinity derived from Argo float observations. JAMSTEC Rep. Res. Dev. 8, 47–59. https://doi.org/10.5918/jamstecr.8.47.
Iida, Y., Kojima, A., Takatani, Y., Nakano, T., Midorikawa, T., Ishii, M., 2015. Trends in *p*CO2 and sea-air CO2 flux over the global open oceans for the last two decades. J. Oceanogr. 71 (6), 637–661. https://doi.org/10.1007/s10872-015-0306-4.
Ishii, M., Inoue, H.Y., Midorikawa, T., Saito, S., Tokieda, T., Sasano, D., Nakadate, A., Nemoto, K., Metzl, N., Wong, C.S., Feely, R.A., 2009. Spatial variability and decadal trend of the oceanic CO2 in the western equatorial Pacific warm/fresh water. Deep Sea Res. Part II 56, 591–606. https://doi.org/10.1016/j.dsr2.2009.01.002.
Ishii, M., Feely, R.A., Rodgers, K.B., Park, G.-H., Wanninkhof, R., Sasano, D., Sugimoto, H., Cosca, C.E., Nakaoka, S., Telszewski, M., Nojiri, Y., Mikaloff Fletcher, S.E., Niwa, Y., Patra, P.K., Valsala, V., Nakano, H., Lima, I., Doney, S.C., Buitenhuis, E.T., Aumont, O., Dunne, J.P., Lenton, A., Takahashi, T., 2014. air-sea CO_2 flux in the Pacific ocean for the period 1990-2009. Biogeosciences 11, 709–734. https://doi.org/10.5194/bg-11-709-2014.
Jiang, M., Chai, F., 2006. Physical control on the seasonal cycle of surface of CO_2 in the equatorial Pacific. Geophys. Res. Lett. 33, L2360. https://doi.org/10.1029/2006GL027195.
Jones, S.D., Le Quéré, C., Rödenbeck, C., 2012. Autocorrelation characteristics of surface ocean $pCO_2$and air-sea CO_2 fluxes. Glob. Biogeochem. Cycles 26, GB2042. https://doi.org/10.1029/2010GB004017.
Kanamitsu, M., Ebisuzaki, W., Woollen, J., Yang, S.-K., Hnilo, J.J., Fiorino, M., Potter, G. L., 2002. NCEP-DOE AMIP-II Reanalysis (R-2). Bull. Am. Meteorol. Soc. 83, 1631–1643. https://doi.org/10.1175/BAMS-83-11-1631.
Kuragano, T., Kamachi, M., 2000. Global statistical space-time scales of oceanic variability estimated from the TOPEX/POSEIDON altimeter data. J. Geophys. Res. 105, 955–974. https://doi.org/10.1029/1999JC900247.
Landschützer, P., Gruber, N., Bakker, D.C.E., Schuster, U., 2014. Recent variability of the global ocean carbon sink. Glob. Biogeochem. Cycles 28, 927–949. https://doi.org/10.1002/2014GB004853.
Landschützer, P., Gruber, N., Bakker, D.C.E., 2016. Decadal variations and trends of the global ocean carbon sink. Glob. Biogeochem. Cycles 30. https://doi.org/10.1002/2015GB005359.
Lee, K., Tong, L.T., Millero, F.J., Sabine, C.L., Dickson, A.G., Goyet, C., Park, G.H., Wanninkhof, R., Feely, R.A., Key, R.M., 2006. Global relationships of total alkalinity with salinity and temperature in surface waters of the world's oceans. Geophys. Res. Lett. 33, L19605. https://doi.org/10.1029/2006GL027207.
Lewis, E., Wallace, D.W.R., 1998. Program Developed for CO2 System Calculations. ORNL/CDIAC-105. Carbon Dioxide Information Analysis Center. Oak Ridge National Laboratory, U.S. Department of Energy, Oak Ridge, Tennessee.
Lueker, T.J., Dickson, A.G., Keeling, C.D., 2000. Ocean pCO_2 calculated from dissolved inorganic carbon, alkalinity, and equations for K1 and K2: validation based on laboratory measurements of CO_2 in gas and seawater at equilibrium. Mar. Chem. 70, 105–119. https://doi.org/10.1016/S0304-4203(00)00022-0.
Meyer, J., Löscher, C.R., Lavik, G., Riebesell, U., 2017. Mechanisms of P* reduction in the eastern tropical South Pacific. Front. Mar. Sci. 4, 1–12. https://doi.org/10.3389/fmars.2017.00001.
Mantua, N.J., Hare, S.R., Zhang, Y., Wallace, J.M., Francis, R.C., 1997. A Pacific Interdecadal climate oscillation with impacts on salmon production. Bull. Amer. Meteor. Soc. 78, 1069–1079. https://doi.org/10.1175/1520-0477(1997)078<1069:APICOW>2.0.CO;2.
McPhaden, M.J., Picaut, J., 1990. El Niño-Southern Oscillation displacements of the western equatorial Pacific warm pool. Science 250, 1385–1388. https://doi.org/10.1126/science.250.4986.1385.
Murray, F.W., 1967. On the computation of saturation vapor pressure. J. Appl. Meteorol. 6, 203–204. https://doi.org/10.1175/1520-0450(1967)006<0203:OTCOSV>2.0.CO;2.
Nakaoka, S., Telszewski, M., Nojiri, Y., Yasunaka, S., Miyazaki, C., Mukai, H., Usui, N., 2013. Estimating temporal and spatial variation of ocean surface pCO_2 in the North Pacific using a self-organizing map neural network technique. Biogeosciences 10, 6093–6106. https://doi.org/10.5194/bg-10-6093-2013.
Nigam, S., Chao, Y., 1996. Evolution dynamics of tropical ocean-atmosphere annual cycle variability. J. Clim. 9, 3187–3205. https://doi.org/10.1175/1520-0442(1996)009<3187:EDOTOA>2.0.CO;2.
Oka, E., Katsura, S., Inoue, H., Kojima, A., Kitamoto, M., Nakano, T., Suga, T., 2017. Long-term change and variation of salinity in the western North Pacific subtropical gyre revealed by 50-year long observations along 137°E. J. Oceanogr. 73, 479–490.
Olsen, A., Key, R.M., van Heuven, S., Lauvset, S.K., Velo, A., Lin, X., Schirnick, C., Kozyr, A., Tanhua, T., Hoppema, M., Jutterström, S., Steinfeldt, R., Jeansson, E., Ishii, M., Pérez, F.F., Suzuki, T., 2016. The Global Ocean Data Analysis Project version 2 (GLODAPv2) – an internally consistent data product for the world ocean. Earth Syst. Sci. Data 8, 297–323. https://doi.org/10.5194/essd-8-297-2016.
Patra, P.K., Maksyutov, S., Ishizawa, M., Nakazawa, T., Takahashi, T., Ukita, J., 2005. Interannual and decadal changes in the sea-air CO2 flux from atmospheric CO2 inverse modelling. Glob. Biogeochem. Cycles 19, GB4013. https://doi.org/10.1029/2005GL025403.
Quay, P.D., Stutsman, J., Feely, R.A., Juranek, L.W., 2009. Net community production rates across the subtropical and equatorial Pacific Ocean estimated from air-sea δd13C disequilibrium. Glob. Biogeochem. Cycles 23, GB2006. https://doi.org/10.1029/2008gb003193.
Rasmusson, E.M., Carpenter, T.H., 1982. Variations in tropical sea surface temperature and wind associated with the Southern oscillation/El Niño. Mon. Weather Rev. 110, 354–384. https://doi.org/10.1175/1520-0493(1982)110<0354:VITSST>2.0.CO;2.
Rayner, N.A., Parker, D.E., Horton, E.B., Folland, C.K., Alexander, L.V., Rowell, D.P., Kent, E.C., Kaplan, A., 2003. Global analyses of sea surface temperature, sea ice, and night marine air temperature since the late nineteenth century. J. Geophys. Res. 108, 4407. https://doi.org/10.1029/2002JD002670.
Reynolds, R.W., Smith, T.M., 1994. Improved global sea surface temperature analysis using optimum interpolation. J. Clim. 7, 929–948. https://doi.org/10.1175/1520-0442(1994)007<0929:IGSSTA>2.0.CO;2.
Rödenbeck, C., Bakker, D.C.E., Gruber, N., Iida, Y., Jacobson, A.R., Jones, S., Landschützer, P., Metzl, N., Nakaoka, S., Olsen, A., Park, G.-H., Peylin, P., Rodgers, K.B., Sasse, T.P., Schuster, U., Shutler, J.D., Valsala, V., Wanninkhof, R., Zeng, J., 2015. Data-based estimates of the ocean carbon sink variability - first results of the Surface Ocean pCO2 Mapping intercomparison (SOCOM). Biogeosciences 12, 7251–7278. https://doi.org/10.5194/bg-12-7251-2015.
Strutton, P.G., Evans, W., Chavez, F.P., 2008. Equatorial Pacific chemical and biological variability, 1997–2003. Glob. Biogeochem. Cycles 22, GB2001. https://doi.org/10.1029/2007GB003045.
Sutton, A., Feely, R., Chris, S., McPhaden, M.J., Takahashi, T., Chávez, F.P., Friederich, G.E., Mathis, J.T., 2014. Natural variability and anthropogenic change in equatorial Pacific surface ocean pCO2 and pH. Glob. Biogeochem. Cycles 28, 131–145. https://doi.org/10.1002/2013GB004679.

Sweeney, C., Gloor, E., Jacobson, A.R., Key, R.M., McKinley, G., Sarmiento, J.L., Wanninkhof, R., 2007. Constraining global air-sea gas exchange for CO_2 with recent bomb ^{14}C measurements. Glob. Biogeochem. Cycles 21, GB2015. https://doi.org/10.1029/2006GB002784.

Takahashi, T., et al., 2009. Climatological mean and decadal change in surface ocean pCO_2, and net sea–air CO_2 flux over the global oceans. Deep Sea Res. Part II 56, 554–577. https://doi.org/10.1016/j.dsr2.2008.12.009.

Takahashi, T., Olafsson, J., Goddard, J.G., Chipman, D.W., Sutherland, S.G., 1993. Seasonal variation of CO_2 and nutrients in the high-latitude surface oceans: a comparative study. Glob. Biogeochem. Cycles 7, 843–878. https://doi.org/10.1029/93GB02263.

Takahashi, T., Stewart, C.S., Sweeney, C., Poisson, A., Metzl, N., Tilbrook, B., Bates, N., Wanninkhof, R., Feely, R.A., Sabine, C., Olafsson, J., Nojiri, Y., 2002. Global sea-air CO_2 flux based on climatologicalsurface ocean pCO_2, and seasonal biological and temperature effects. Deep Sea Res. Part II 49, 1601–1622. https://doi.org/10.1016/S0967-0645(02)00003-6.

Takahashi, T., Sutherland, S.C., Feely, R.A., Cosca, C.E., 2003. Decadal variation of the surface water PCO2 in the western and central equatorial Pacific. Science 302, 852–856. https://doi.org/10.1126/science.1088570.

Takatani, Y., Enyo, K., Iida, Y., Kojima, A., Nakano, T., Sasano, D., Kosugi, N., Midorikawa, T., Suzuki, T., Ishii, M., 2014. Relationships between total alkalinity in surface water and sea surface dynamic height in the Pacific Ocean. J. Geophys. Res. Oceans 119, 2806–2814. https://doi.org/10.1002/2013JC009739.

Tokinaga, H., Xie, S.-P., 2011. Wave- and anemometer-based sea surface wind (WASWind) for climate change analysis. J. Clim. 24, 267–285. https://doi.org/10.1175/2010JCLI3789.1.

Trenberth, K.E., 1997. The definition of El Niño. Bull. Am. Meteorol. Soc. 78, 2771–2777. https://doi.org/10.1175/1520-0477(1997)078<2771:TDOENO>2.0.CO;2.

Valsala, V.K., Roxy, M.K., Ashok, K., Murtugudde, R., 2014. Spatiotemporal characteristics of seasonal to multidecadal variability of pCO2 and air-sea CO_2 fluxes in the equatorial Pacific Ocean. J. Geophys. Res. 119, 8987–9012. https://doi.org/10.1002/2014JC010212.

van Heuven, S., Pierrot, D., Lewis, E., Wallace, D.W.R., 2009. MATLAB Program Developed for CO2 System Calculations, ORNL/CDIAC-105b. Carbon Dioxide Information Analysis Center. Oak Ridge National Laboratory, US Department of Energy, Oak Ridge, Tennessee.

Walker Brown, C., Boutin, J., Merlivat, L., 2015. New insights into fCO_2 variability in the tropical Eastern Pacific Ocean using SMOS SSS. Biogeosciences 12, 7315–7329. https://doi.org/10.5194/bg-12-7315-2015.

Wang, X.J., Christian, J.R., Murtugudde, R., Busalacchi, A.J., 2006. Spatial and temporal variability of the surface water pCO2 and air-sea CO_2 flux in the equatorial Pacific during 1980-2003: a basin-scale carbon cycle model. J. Geophys. Res. 111, C07S04. https://doi.org/10.1029/2005JC002972.

Wang, X.J., Murtugudde, M., Hackert, E., Wang, J., Beauchamp, J., 2015. Seasonal to decadal variations of sea surface pCO_2 and sea-air CO_2 flux in the equatorial oceans over 1984–2013: a basin-scale comparison of the Pacific and Atlantic Oceans. Glob. Biogeochem. Cycles 29, 59–609. https://doi.org/10.1002/2014GB005031.

Wanninkhof, R., 2014. Relationship between wind speed and gas exchange over the ocean revisited. Limnol Oceanogr. Methods 12, 351–362. https://doi.org/10.4319/lom.2014.12.351.

Wanninkhof, R., Park, G.-H., Takahashi, T., Sweeney, C., Feely, R., Nojiri, Y., Gruber, N., Doney, S.C., McKinley, G.A., Lenton, A., Le Quéré, C., Heinze, C., Schwinger, J., Graven, H., Khatiwala, S., 2013. Global ocean carbon uptake: magnitude, variability and trends. Biogeosciences 10, 1983–2000. https://doi.org/10.5194/bg-10-1983-2013.

Weiss, R.F., 1974. Carbon dioxide in water and seawater: the solubility of a non-ideal gas. Mar. Chem. 2, 203–215. https://doi.org/10.1016/0304-4203(74)90015-2.

Wyrtki, K., 1964. Upwelling in the Costa Rica dome. Fish. Bull. 63, 355–372.

Xie, S.-P., Xu, H., Kessler, W.S., Nonaka, M., 2005. Air-sea interaction over the eastern Pacific warm pool: gap winds, thermocline dome, and atmospheric convection. J. Clim. 18, 5–25. https://doi.org/10.1175/JCLI-3249.1.

Yan, X.-H., Ho, C.-R., Zheng, Q., Klemas, V., 1992. Temperature and size variabilities of the western Pacific warm pool. Science 258, 1643–1645. https://doi.org/10.1126/science.258.5088.1643.

Yasunaka, S., Nojiri, Y., Nakaoka, S., Ono, T., Whitney, F.A., Telszewski, M., 2014. Mapping of sea surface nutrients in the North Pacific: basin-wide distribution and seasonal to interannual variability. J. Geophys. Res. 119, 7756–7771. https://doi.org/10.1002/2014JC010318.